第35卷 第4期 焊 接 学 报 Vol. 35 No. 4
2014年4月 TRANSACTIONS OF THE CHINA WELDING INSTITUTION April 2014

大气下热喷涂等离子体电子密度的光谱诊断

孙成琪[1,2]， 高 阳[1]， 杨德明[1]， 陈振宇[1]
(1. 大连海事大学 交通运输装备与海洋工程学院，大连 116026；2. 广东海洋大学 航海学院，湛江 524025)

摘 要：利用直流电弧放电装置产生了大气压下热喷涂等离子体，采用原子发射光谱法测量热喷涂等离子体射流中的辐射强度. 通过 Stark 展宽法，使用 Ar I 谱线在 430 nm 处的 $\Delta\lambda_{1/2}$(谱线的半宽高) 对大气压力下热喷涂等离子体射流中电子密度进行计算，研究了不同氩气流量及不同输入功率对等离子体电子密度的影响；同时使用 Saha 方程计算氩等离子体的电离程度，研究气体流量和电流与氩等离子体电离程度的关系. 结果表明，电子密度和电离程度随着等离子体喷枪输入功率的增加而增加，而随着气体流量增加时，电子密度略有增加而电离程度会减少.

关键词：热喷涂等离子体；发射光谱；电离程度；电子密度
中图分类号：TG 403 **文献标识码**：A **文章编号**：0253－360X(2014)04－0075－04

0 序 言

等离子喷涂中由于热等离子炬的高温、高速以及高传热特性，已经被广泛的应用于各种工程技术领域，形成各种耐磨涂层、耐高温涂层和耐腐蚀涂层等. 尤其是使用性能优越却极其难熔的陶瓷粉末和硬质合金粉末的喷涂问题，在等离子喷涂中得到了很好的解决[1]. 尽管等离子喷涂已经取得了令人瞩目的发展，许多等离子喷涂的基本机理仍然需要进一步的了解，这包括等离子炬的特性研究. 研究等离子喷涂过程中等离子炬基本物理特性对于进一步提高涂层的质量具有重要意义，而等离子炬的电子温度和密度是表征等离子体性质的一个重要参数，这是因为所有的物理、化学过程(包括激发、离化和化学反应) 都与电子密度直接相关，同时这也是热等离子喷涂中研究的热点问题[2]. 热等离子炬电子温度和密度的测量一般使用朗缪尔探针和发射光谱法，其中发射光谱法因其是一种响应速度快、无干扰的原位测量法，成为等离子体诊断中应用最广泛的一种. 发射光谱法通过测量谱线的强度、展宽和频移来计算等离子体的参数，通过分析等离子体发射谱线的 Stark 展宽来测量电子密度，而谱线的展宽又受到辐射原子和离子以及环境等多种因素的影响. 人们对 DC 电弧等离子喷涂中等离子体的温度和速度进行了大量的研究，然而通过 Ar I 谱线(非类氢谱线) 来计算电子温度的研究还比较有限.

收稿日期：2012－12－20
基金项目：国家自然科学基金资助项目(51172033)

Joshi 等人[3] 通过使用 H_β 谱线和 Ar I 谱线的 Stark 展宽和经验公式分别计算了直流电弧等离子喷涂中等离子炬的电子密度并进行了对比. Yugeswaran 等人[4] 对非氢谱线下的电子密度进行了测量，并对等离子体的离子化程度进行了计算. 潘成刚等人[5] 通过傅里叶变换法从测量光谱谱线中分离出 Stark 展宽，并计算电子密度. 董丽芳等人[6] 测量了大气压力下等离子炬的 H_β 谱线和 Ar I(696.54 nm) 谱线，并通过反卷积方法分离出其相应的 Stark 展宽，计算等离子体的表层和内部的电子密度.

文中研究了不同氩气流量、不同等离子喷涂功率条件下的电子密度，其计算采用氩的原子谱线 Ar I (430 nm) 的 Stark 展宽. 在保持氩气流量不变时，改变等离子体的喷涂功率，计算在距离喷嘴出口 10 mm 处得等离子体电子密度的变化情况. 同时通过发射光谱强度对比法计算等离子体的电子温度，由于大气压力下等离子喷涂时，等离子体处于局域热力学平衡状态，所以测量的电子温度与重离子温度和激发温度相等，根据 Saha 方程，可以计算出热等离子体的离子化程度.

1 试验装置和测量方法

1.1 试验设备与测量装置

试验中使用大连海事大学热喷涂研究中心的大气等离子喷涂系统，喷枪是由水冷的涂钍钨阴极和铜阳极喷嘴构成. 图 1 为工作中的等离子体焰流，等离子体电弧由气体的持续供给来保持，一般来说氩气是很好的稳定等离子体电弧的气体，同时引弧

的电压比较低[7]. 文中研究纯氩气条件下,距离喷嘴出口轴向 10 mm 处,输入功率、气体流量对等离子炬电子密度的影响,其详细喷涂参数见表 1.

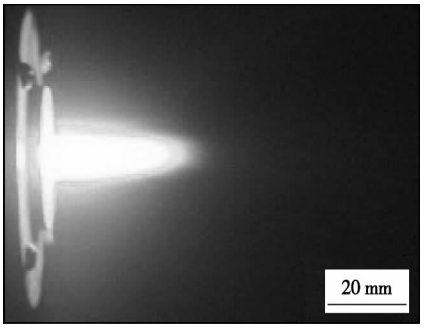

图 1 等离子体焰流

Fig. 1 Photo of plasma jet

表 1 试验条件

Table 1 Experiment conditions

试验编号	电流 I/A	电压 U/V	气体流量 q/(L·min^{-1})
1	100	23	25
2	150	24	30
3	200	26	35
4	250	27	40

图 2 为测量等离子体电子温度和电子密度的试验装置的系统. 使用 AvaSpec-2048-4-USB2 光纤光谱仪采集等离子体焰流的光学信号,测量分辨率为 0.2 nm,测量波长范围为 200 ~ 1 020 nm,积分时间为 1.1 ~ 60 000 ms,采样速度为 1.1 ms/次,带有 CCD 探测器,分辨率为 4 × 2 048 像素. 400 μm 的光纤探头放置在距离喷枪轴线 50 cm、对准等离子喷枪出口 10 mm 处. 为保证测量结果的准确性,试验前对光谱诊断设备进行必要的调试和校正,使用标准光源 AvaLight-HAL 卤钨灯对光谱仪进行标定. 测量时,通过改变 CCD 探测器的读出频率即积分时间(也称为曝光时间)保证 4 个通道中获得的信号强度

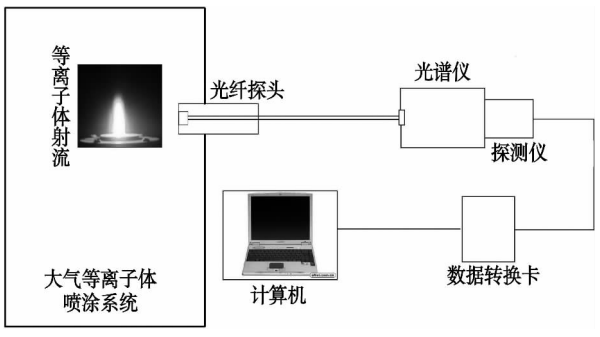

图 2 光谱测量系统

Fig. 2 Setup of emission spectroscopy diagnostics

不出现饱和,为了测量数据具有可比性,4 个通道测量的积分时间都为 1.05 ms,为了降低信噪比的影响,平均扫描次数选择 100 次. 使用 Plasus SpecLine 软件对测量的光谱数据进行分析和标定,确定不同原子的谱线,其软件中所使用的数据库来自美国国家标准与技术研究院. 图 3 为在氩气流量 30 L/min,电流 250 A,功率 6 kW 条件下,所采集的等离子体光谱信息,光谱图谱中显示了 Ar 原子辐射光谱谱线在 ArI(430 nm)处的辐射强度.

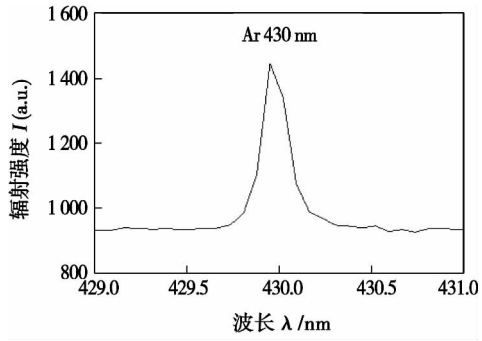

图 3 ArI 的发射光谱谱线轮廓

Fig. 3 Profile of ArI spectrum

1.2 测量原理

任何谱线都不会是绝对单色的,而是具有一定的波长范围. 谱线轮廓所覆盖的波长范围,就是谱线的宽度. 原子谱线的线型和线宽是大量物理条件的信息源,辐射原子或离子在周围电子和离子的扰动下而引起的谱线 Stark 展宽,是测定等离子体电子密度的一种有效方法.

正在发射光子的粒子由于受到周围带电粒子的影响造成的谱线增宽现象叫 Stark 效应. 一般说来,谱线的加宽主要有自然加宽、Doppler 加宽、Stark 加宽、中性粒子引起的碰撞加宽以及采用光谱仪时由仪器引起的仪器加宽. 在等离子体中由于存在大量电子和离子,快速电子和慢速离子形成电场,使 Stark 加宽成为主要加宽机制之一. 而这一展宽主要取决于等离子体的电子密度,与温度的关系不大. 更重要的是 Stark 展宽与等离子体是否处于局部热力学平衡状态(LTE)无关,这就极大的扩展了其应用范围.

在高密度等离子体中,非氢原子主要是二次 Stark 效应,它导致的谱线的展宽($\Delta\lambda_{1/2}$)是电子密度和电子温度的一个复杂函数,可表示为

$$\Delta\lambda_{1/2} = 2\times10^{-16}\omega n_e \left[1 + 1.75\times10^{-4} n_e^{\frac{3}{4}} \alpha\left(1 - 0.068 n_e^{\frac{3}{4}} / T_e^{\frac{1}{2}}\right)\right] \quad (1)$$

式中: ω 为电子碰撞半宽; α 为离子加宽参数; n_e 为电子密度; T_e 为电子温度. 对于 ArⅠ 谱线,通过使用 ArⅠ 谱线在 430 nm 处的 $\Delta\lambda_{1/2}$ 来计算电子的密度 n_e,ω 和 α 的值由 Griem 等人给出,但是至今对于 ω 和 α 的值还存在着争论,而且对比不同的参数值,其电子密度的计算值误差在 ± 15% ~ ± 20%. 另外 Joshi 等人[3] 给出了使用 ArⅠ 谱线在 430 nm 处的 $\Delta\lambda_{1/2}$ 来计算电子密度的修正公式,即

$$\lg n_e = 17.432 + 0.662\lg\Delta\lambda_{1/2} \quad (2)$$

计算 5 和 10 kW 时,等离子体电子密度沿喷嘴出口轴向的变化,与由式(1)的结果对比发现,两者的计算结果基本一致.

研究热等离子体的电离程度对于了解其射流特性具有重要意义. 热喷涂等离子体中粒子之间的碰撞可以是弹性的也可以是非弹性的. 对于纯氩等离子体,在温度足够高时(如 1 标准大气压,高于 8 000 K)时,将出现一次电离 - 复合反应,即

$$Ar \Leftrightarrow Ar^+ + e \quad (3)$$

温度更高时(如 1 标准大气压,高于 20 000 K),一次电离的 Ar^+ 还会进一步电离 - 复合反应,即

$$Ar^+ \Leftrightarrow Ar^{++} + e \quad (4)$$

热喷涂等离子炬中电离以氩的一次电离为主. 处于完全热力学平衡或局域热力学平衡态的等离子体中,在给定的压力和温度下,其组分可以有理想气体定律、电中性条件和化学平衡关系确定[4]. 因此重离子温度和电子密度已知后,热喷涂等离子炬的电离程度可以通过 Saha 方程来计算,氩等离子体的电离度(D_i)为

$$D_i = (3\times10^{21}/n_e)(T)^{3/2}\exp(-V_i/T) \quad (5)$$

式中: T 为重离子的温度; V_i 为氩原子的一次电离能.

2　试验结果与讨论

图 4 为在距离喷嘴出口 10 mm 处,4 种电流条件下,氩气流量变化对电子密度的影响. 在低电流时,即电流保持 100 A 的情况下,氩气流量从 25 L/min变化到 40 L/min 时,电子密度从 6.64×10^{16} /cm^{3}增加到 7.62×10^{16}/cm^3,而在电流保持 200 A 不变时,电子密度基本不随氩气流量的变化而变化,为 9.00×10^{16}/cm^3 左右,电流保持在 250 A 时,电子密度为 1.00×10^{17}/cm^3 左右. 由此可见,在电流较小时,氩气流量增加会增加电子的密度,随着电流的增加,氩气流量变化对电子密度几乎没有什么影响. 图 5 为电流对电子密度的影响,在保持氩气流量 25 L/min 不变时,随着电流的增加,电子密度从 6.64×10^{16}/cm^3 逐渐增加到 1.03×10^{17}/cm^3.

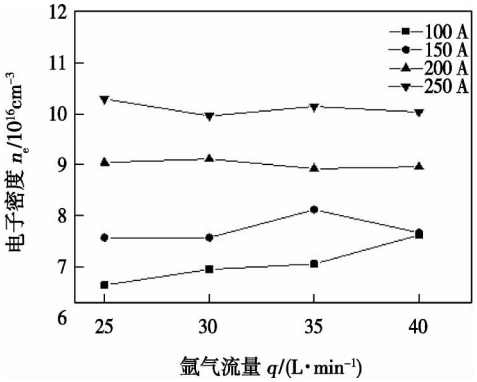

图 4　电子密度随气体流量和电流变化曲线

Fig. 4　Evolution of electron density with gas rate and current intensity

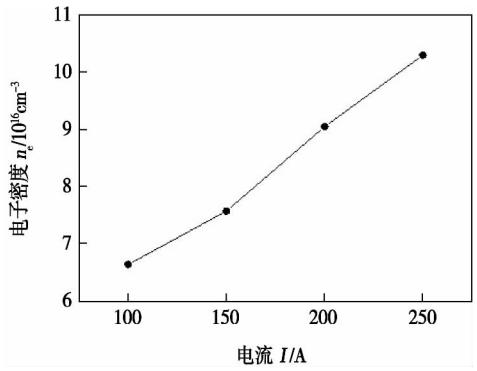

图 5　电流变化对电子密度的影响

Fig. 5　Effect of current intensity on electron density

图 6 为功率对电子密度的影响,在保持氩气流量 35 L/min 时,输出功率由 2.6 kW 变化到 6.5 kW 时,等离子体的电子密度由 6.95×10^{16}/cm^3 增加到 9.96×10^{16}/cm^3,从计算可知电子密度与谱线的展宽成正比,增加电流热喷涂等离子体的输出功率,原子的电离和碰撞会增强.

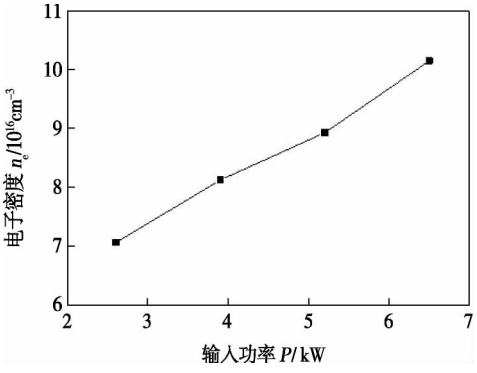

图 6　等离子体输入功率对电子密度的影响

Fig. 6　Effect of plasma power on electron density

图7给出了在距离喷嘴出口10 mm处,4种氩气流量条件下,不同输入电流对热喷涂等离子体电离度的影响. 等离子体的电离过程主要是由等离子体射流的温度、电子密度和气体密度来决定的,从图7可以看出等离子体电离度随等离子体射流输入电流的增加而增加,这是由于电流增加,等离子体的输入功率增加,等离子体的温度升高,Ar原子的电离也会增多. 在保持电流不变时,随气体流量的增加而略有减小,氩气流量增加时,由于总的能量不变,等离子体的温度会降低,这样就导致Ar原子的电离机会减少.

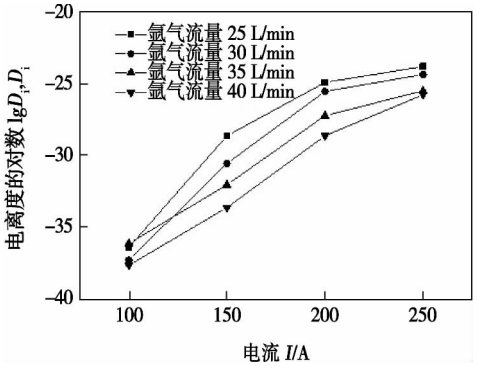

图7 气体流量和电流变化对等离子体电离度的影响

Fig. 7 Effect of gas rate and current intensity on degree of ionization of a plasma jet

3 结 论

(1) 在纯氩气条件下,电流较小时随着氩气流量的增加,等离子体的电子密度略有增加,电流达到200 A以上时,氩气的流量对等离子体的电子密度几乎没有影响.

(2) 在保持氩气流量不变时,电子密度随着电流和功率的增加而急剧增加.

(3) 热喷涂等离子体的电离度与电流和氩气流量有关,随着电流的增加Ar原子的一次电离度会增加,随着氩气流量的增加电离度略有减少.

参考文献:

[1] Pawlowski L. The science and engineering of thermal spray coatigs [M]. France: John Wiley & Sons, 2008.

[2] Pfender E. Thermal plasma technology where do we stand and where are we going [J]. Plasma Chemistry and Plasma Processing, 1999, 19(1): 1-31.

[3] Joshi N K, Sahasrabudhe S N, Sreekumar K P, *et al*. Axial variation of electron number density in thermal plasma spray jets [J]. The European Physical Journal D, 2003, 26(2): 215-219.

[4] Yugeswaran S, Selvarajan V. Electron number density measurement on a DC argon plasma jet by stark broadening of Ar Ⅰ spectral line [J]. Vacuum, 2006, 81(3): 347-352.

[5] 潘成刚, 华学明, 张 旺, 等. 傅里叶变换法计算焊接电弧光谱Stark展宽研究 [J]. 光谱学与光谱分析, 2012, 32(7): 1739-1743.
Pan Chenggang, Hua Xueming, Zhang Wang, *et al*. Calculating the stark broadening of welding arc spectra by fourier transform method [J]. Spectroscopy and Spectral Analysis, 2012, 32(7): 1739-1743.

[6] 董丽芳, 刘为远, 杨玉杰, 等. 大气压等离子体炬电子密度的光谱诊断 [J]. 物理学报, 2011, 60(4): 1-6.
Dong Lifang, Liu Weiyuan, Yang Yujie, *et al*. Spectral diagnostics of electron density of plasma torch at atmospheric presure [J]. Acta Physics Science, 2011, 60(4): 1-6.

[7] 安连彤, 高 阳. 阳极弧根位置对热喷涂等离子体喷枪特性的影响 [J]. 焊接学报, 2005, 26(6): 31-34.
An Liantong, Gao Yang. Effect of anode arc root position on the characteristics of the thermal spray plasma torch [J]. Transactions of the China Welding Institution, 2005, 26(6): 31-34.

[8] 陈 熙. 热等离子体的传热与流动 [M]. 北京: 科学出版社, 2009.

作者简介: 孙成琪,男,1979年出生,博士研究生,讲师. 主要从事热等离子体射流特性的研究. 发表论文5篇. Email: 46792393@qq.com

通讯作者: 高 阳,男,教授. Email: gaoyang@dlmu.edu.cn

quently at the stage of crack nucleation. The increase of inclusions with large size was the main reason of the appearance of quasi-cleavage fracture and the decrease of impact absorbed energy.

Key words: high strength steel; deposited metal; mechanical property; microstructure

Influence of process parameters on the cracking rate and morphology of the laser melting and quenching zone in vermicular graphite cast iron ZHENG Ziyun, MA Bing, FENG Shengqiang, LIU Guang (Ningbo Branch of China Academy of Ordnance Science, Ningbo 315103, China). pp 58 – 62

Abstract: Laser melting and quenching experiments were conducted on vermicular graphite cast iron by employing 3 kW solid fiber laser. The cracking rate in the quenching zone, the morphology of the melting zone, microhardness and microstructure were analyzed. The results show that, at a given flow rate of shielding gas, increasing the laser power or reducing the scanning speed could facilitate the reduction of cracking rate in the quench zone. When the laser power was constant, the optimum flow rate of the shielding gas changed with the scanning speed. With the increase of laser power, the morphology of the quenching zone extended to the substrate. The morphology extended vertically and horizontally in the melting zone, and then in other directions. After that, it extended vertically and horizontally, and cycled. The gross area of the melting zone increased consequently, and the morphology of the quenching zone changed from flat to calyptra.

Key words: laser melting and quenching; vermicular graphite cast iron; cracking rate; melting zone; morphology

Microstructure characteristics of RuTi/1060Al fusion-brazed joint by pulsed gas metal arc welding WEI Shouzheng, LI Yajiang, WANG Juan, ZHANG Pengfei (Key Laboratory for Liquid-Solid Structural Evolution & Processing of Materials (Ministry of Education), Shandong University, Jinan 250061, China). pp 63 – 66

Abstract: Pulsed gas metal arc welding of RuTi titanium alloy to 1060 aluminum was conducted. The microstructure in weld zone of RuTi Ti/1060Al joint was examined by scanning electron microscope (SEM) fitted with energy-dispersive spectrometer (EDS). Elemental distribution and precipitated phase in weld zone and transition region on Ti alloy side were analyzed by EDS. The weld zone was composed of α-Al dendrites and eutectic α-Al + Si structures. The eutectic α-Al + Si structures distributed along the boundaries of α-Al dendrites. Striped or block $Ti(Al,Si)_3$ intermetallics appeared in the weld zone. A serrated transition region mainly containing $Ti(Al,Si)_3$ intermetallics was formed between the RuTi titanium alloy and the weld zone. The width of the Ti/Al transition region was less than 10 μm. With the increasing of welding heat input, the Ti/Al transition region presented a rod-like appearance. The heat-affected zone (HAZ) of RuTi titanium alloy consisted of acicular α″ and lath α′ martensite. The average microhardness in the HAZ was about 2.16 – 2.65 GPa.

Key words: RuTi titanium alloy; 1060 aluminum; pulsed gas metal arc welding; microstructure; precipitated phase

Uniform design and optimization of active flux for A-TIG welding of AZ31B magnesium alloy DU Xianchang, WANG Yi, GUO Shulan, YANG Chunguang (School of Mechanical and Electrical Engineering, Changchun Institute of Technology, Changchun 130012, China). pp 67 – 70

Abstract: Active fluxes with four components (TiO_2, $SrCl_2$, ZrO_2 and Y_2O_3) were developed based on the requirements of A-TIG welding of AZ31B magnesium alloy on active fluxes, including weld penetration, weld appearance, mechanical properties and reinforcement mechanism of weld, process feasibility and non-toxic etc. The composite active fluxes were designed by uniform design method. A mathematical model was established according to the weld penetration depth and weld appearance. The optimized ingredients of active fluxes were determined and verified through the comparative analysis with different mathematical models. The results show that the maximum penetration could be obtained with good weld appearance and the welded joint had excellent mechanical properties, when the active fluxes was designed with the proposed uniform design method.

Key words: magnesium alloy; active flux; uniform design

Analyses of reheat cracking sensitivity and test methods for 07MnNiVDR steel LIU Junsong[1,2], CHEN Xuedong[2], BU Huaquan[2] (1. School of Materials Science and Engineering, Hefei University of Technology, Hefei 230009, China; 2. Hefei General Machinery Research Institute, Hefei 230031, China). pp 71 – 74

Abstract: Reheat cracking sensitivity of the quenched and tempered high strength 07MnNiVDR steel was investigated with methods, such as low strain rate tensile test at high temperature after thermal simulation, Charpy pendulum impact test, implant test and small Tekken test. The thermal simulation results show that the steel was insensitive to reheat cracking with low welding heat input, but sensitive with high welding heat input and the sensitive temperature was around 600 ℃. Implant test also indicates that the steel had risk of reheat cracking to some extent, with sensitive temperature of about 600 ℃. The results of thermal simulation test and implant test were consistent with each other, while small Tekken test was not suitable for testing reheat cracking sensitivity. Low stain rate tensile test after thermal simulation was a practical and effective method for reheat cracking sensitivity assessment. The critical stress of implant test was important for engineering practice. Post-weld heat treatment of this steel joint should be prudent, although no apparent reheat cracking was found in small Tekken test.

Key words: high strength steel; reheat cracking; welding; thermal simulation

Spectral diagnostics of electron number density in plasma jet under atmosphere thermal plasma spray SUN Chengqi[1,2], GAO Yang[1], YANG Deming[1], CHEN Zhenyu[1] (1. School of Transportation Equipment and Ocean Engineering, Dalian Maritime University, Dalian 116026, China; 2. Maritime

College, Guangdong Ocean University, Zhanjiang 524025, China). pp 75 – 78

Abstract: A direct current atmospheric plasma spray was conducted at different power levels and flow rates of argon plasma gas. In this paper, electron number density of the plasma jet was determined using $\Delta\lambda_{1/2}$ of the Ar I (430 nm) line, and the effect of different power levels and flow rates of Ar plasma gas on the electron number density in the thermal spray plasma jet was investigated. Meanwhile, the degree of ionization of Ar atom was analyzed using Saha equation, and the relations between the degree of ionization, the gas flow and arc electric current were discussed. The results show that the electron number density increased with increasing the plasma input power and Argon content of the plasma gas, while the degree of ionization increased with the increase of the plasma power but decrease of the Argon flow rate.

Key words: thermal spray plasma; emission spectroscopy; degree of ionization; electron number density

Non-linear influence of welding thermal effect on dynamic performance of structure CHEN Zhanglan[1], YE Jiawei[2] (1. Marine Engineering Institute, Jimei University, Xiamen 361021, China; 2. School of Civil Engineering and Transportation, South China University of Technology, Guangzhou 510640, China). pp 79 – 82

Abstract: The influence of welding thermal effect on the dynamic performance of complex structure was proposed and confirmed by both formula derivation and numerical solution by finite element analysis method. Based on constitutive relation including initial stress and strain, the stiffness matrix considering the welding thermal effect was derived by employing the principal of virtual work. Then modified characteristic equation of modal analysis including geometric non-linear, stress stiffening and welding thermal effect was established. Modal analysis by taking a ship hull block as the example was performed to testify the derived equation and the first natural frequencies were extracted. The comparisons of different first natural frequencies induced by different levels of welding residual stress exhibited that the welding thermal effect obviously influenced the vibration performance of hull block by changing natural vibration frequencies of the structure. Especially, certain value of welding residual stress could even lower the first natural frequency nearly to wave frequency. The results show that the welding thermal effect played an important role in the dynamic performance of structure and could not be neglected in vibration analysis.

Key words: welding thermal effect; stiffness matrix; geometric non-linear; hull block; dynamic performance

Laser-TIG-adhesive hybrid welding of magnesium to steel with Ni alloy interlayer WANG Hongyang, ZHANG Zhaodong, CAO He (Key Laboratory of Liaoning Advanced Welding and Joining Technology, Dalian University of Technology, Dalian 116024, China). pp 83 – 86

Abstract: Laser-TIG-adhesive hybrid welding was carried out to join AZ61 magnesium alloy to Q235 steel with Ni interlayer. Weld surface appearance, microstructure and distribution of alloying elements in the fusion zone were investigated. The experimental results indicate that the welding heat input was the key factor on the weld surface formation when the thickness of adhesive was constant. The seam was mainly composed of Mg, Fe and Ni. In the fusion zone, the addition of adhesive reinforced the liquidity and promoted the reaction among molten metals. The AZ61 magnesium alloy and steel were metallurgically bonded, and the liner load capacity of the resultant joint increased. The comprehensive performance of the joint was improved.

Key words: adhesive; magnesium alloy; steel; laser-TIG hybrid welding

Visco-elastic-plastic constitutive model for welding of A7N01-T6 aluminum alloy SONG Kuijing[1], WEI Yanhong[1,2], DONG Zhibo[1], MA Rui[3], ZHAN Xiaohong[2], ZHENG Wenjian[1], FANG Kun[1] (1. State Key Laboratory of Advanced Welding and Joining, Harbin Institute of Technology, Harbin 150001, China; 2. School of Materials Science and Technology, Nanjing University of Aeronautics and Astronautics, Nanjing 210016, China; 3. Beijing Power Machinery Research Institute, Beijing 100074, China). pp 87 – 90, 94

Abstract: A visco-elastic-plastic constitutive model for welding of A7N01-T6 aluminum alloy was established, considering the welding thermal temperature and deformation history. The model used elastic-mixed hardening plastic and creep equation to describe the strain hardening at low temperatures and strain softening at high temperatures, respectively. And it was applied for finite element numerical simulation of the welding process. Based on the established constitutive model, the welding residual stress and strain agreed well with the theoretical results. Compared to the ideal temperature dependent elastic-plastic model, strain hardening at low temperatures and strain softening at high temperatures had combined effect that led to invariable welding residual stress. Due to strain softening at high temperatures, the overall longitudinal residual compressive plastic strain and the maximum deformation of welding sheet were much larger using the newly proposed model.

Key words: constitutive model; secondary development; strain hardening; strain softening; welding residual stress and deformation

Fatigue failure analysis of 6061-T6 aluminum alloy refilled friction stir spot welding ZHU Xiaogang, WANG Lianfeng, QIAO Fengbin, GUO Lijie (Shanghai Aerospace Equipments Manufacturer, Shanghai 200245, China). pp 91 – 94

Abstract: Fatigue test was carried out on refilled friction stir spot welding joints of 6061-T6 aluminum alloy to identify the reason for fatigue failure, and the S-N curve and conditional fatigue limit were obtained at test load of 1.5 kN. The microstructure and fatigue fracture were examined by scanning electron microscope (SEM), and the fatigue mechanism and fatigue fracture features were investigated. The results show that the main reason for fatigue failure of refilled friction stir spot welding of 6061-T6 aluminum alloy was the hook in the joint and serious stress concentration at notch tip of the boundary between the upper and